eV-TEM: transmission electron microscopy with few-eV electrons

Geelen, D.

Citation

Geelen, D. (2018, May 31). *eV-TEM: transmission electron microscopy with few-eV electrons*. *Casimir PhD Series*. Retrieved from https://hdl.handle.net/1887/63484

Version:	Not Applicable (or Unknown)
License:	Licence agreement concerning inclusion of doctoral thesis in the Institutional Repository of the University of Leiden
Downloaded from:	https://hdl.handle.net/1887/63484

Note: To cite this publication please use the final published version (if applicable).

Cover Page

Universiteit Leiden

The handle http://hdl.handle.net/1887/63484 holds various files of this Leiden University dissertation.

Author: Geelen, D.
Title: eV-TEM: transmission electron microscopy with few-eV electrons
Issue Date: 2018-05-31

Chapter 6

Catastrophes in Low-Energy Electron Resist Exposures*

THE ESCHER SETUP allows us to study the interactions between **L**ow-**E**nergy **E**lectrons (LEE) and matter. Such interactions play an important role in the effects of ionizing radiation in many areas of science, technology, and medicine. Upon the absorption of high-energy electromagnetic radiation (i.e. **U**ltra**V**iolet (UV), EUV (**E**xtreme **U**ltra**V**iolet), X-ray, or γ-radiation) high-energy electrons are released in a material. These electrons generate a cascade of many lower-energy electrons [2]. While these LEE give rise to most chemical and physical changes, their interactions with soft materials are not well studied or understood. Recently, this has become especially relevant now that the semiconductor industry is working on the development of EUV technology in photolithography.

To reach a resolution < 10 nm with photolithography, the resist exposure needs to be extremely well understood. As discussed in chapter 1, the electron mean free path universal curve implies that low-energy electrons have long mean free paths and are therefore expected to travel away from the irradiated region. Because such very low-energy electrons may also expose the resist, this has two obvious consequences: On the one hand this effect reduces the resolution of the exposure. This is referred to as edge blurring. On the other

*The findings in this chapter have been published in [1].

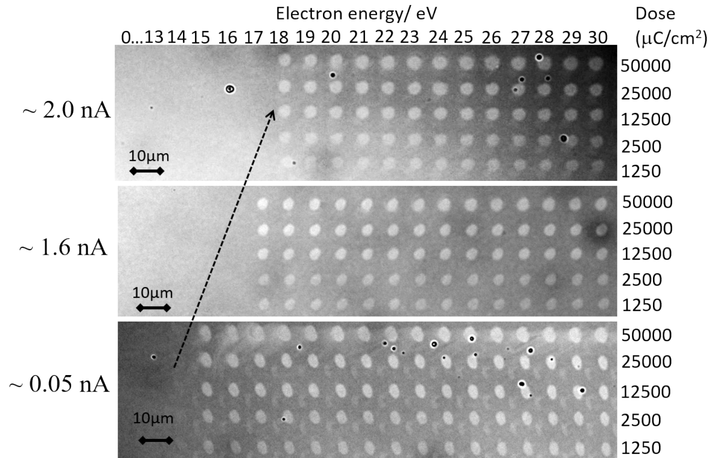

Figure 6.1: Optical microscope micrograph of low-energy electron exposures on a 20 nm thick layer of PMMA with different beam currents and doses. The resist is illuminated with electrons of a certain energy until the required dose is delivered. After this, the beam is blanked and the sample moved to a new position so that a new, pristine, region of PMMA can be exposed. We observe an energy threshold below which the resist is not exposed. This energy threshold shifts to a lower energy when the beam current is reduced.

hand, generation of secondary electrons can make the lithography process more efficient. When a photon affects the resist over an extended area due to the generation of LEE, fewer photons are needed to expose the resist, making the illumination process faster.

To study the effect of low-energy electrons we irradiate a thin layer of **P**oly(**M**ethyl **M**eth**A**crylate) (PMMA) with LEE in the energy range of $0-50$ eV [3]. The radiation chemistry of PMMA has been well studied and irradiation leads to scission of the polymer chains and the removal of side groups [4–9]. PMMA therefore serves as a good starting point to investigate how to study radiation damage in LEEM.

6.1 Low-energy electron exposure of PMMA

In this experiment we investigate the effects of electron irradiation with different electron energy E_0, dose, and beam current I_0. For this a 20 ± 4 nm layer of PMMA is spin coated on a silicon substrate, which is loaded in the ESCHER instrument. For each exposure the PMMA is irradiated with a $5\ \mu$m diameter beam until the required electron dose has been delivered. After the exposure the electron beam is blanked and the sample moved to a new position such that a new area with pristine PMMA can be exposed with another dose, energy, and/or current. With all exposures complete, the sample is removed from the instrument and developed in 1:3 isopropyl alcohol/methyl isobutyl ketone developer for 1 minute.

The results of this experiment are presented in figure 6.1. This shows an optical microscope image of the exposed areas of resist with three different beam currents, ~ 2.0 nA, ~ 1.6 nA, and ~ 0.05 nA. The areas where the radiation dose and energy is sufficient to develop the resist show up as bright spots in the micrograph. From this figure it can be clearly seen that the resist only develops above a certain electron energy threshold, which depends on the beam current. For higher beam currents a higher threshold energy is observed. This beam current dependence suggests that the threshold is not related directly to the electron energy. We do not observe a strong dose dependence.

At first sight it seems counterintuitive that at larger beam currents a higher electron energy is necessary to expose the resist. In the next section we are able to describe our observations with a charging model. We find that secondary electron emission and the changing properties of the resist due to radiation damage (secondary electron emission coefficient and conductance) should also be included in our model.

6.2 Charging model

We can explain the shifting threshold effect with a model that is based on charging of the PMMA layer. When the electron beam with current I_0 impinges on the sample, the PMMA surface will charge to a potential $V_p = V_{substrate} - V_{surface}$ (see figure 6.2a). The current density through the

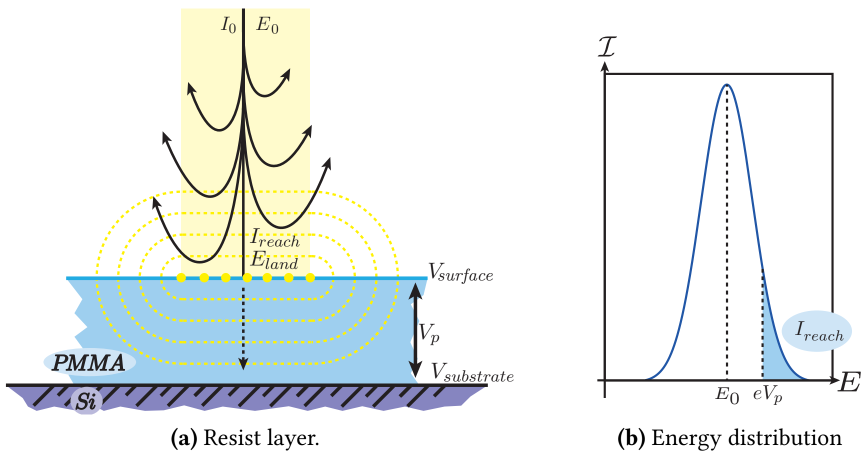

(a) Resist layer.

(b) Energy distribution

Figure 6.2: Schematic representation of the charging model to explain the energy threshold observed in figure 6.1. **(a)** Electron irradiation of the PMMA layer with an electron beam current I_0 with energy E_0. Since the resist is a poor conductor the electrons charge the PMMA surface up to a potential difference V_p. This voltage causes a current to flow through the PMMA layer to the Si substrate (indicated by the dashed line, the arrow points in the direction the electrons flow). Incoming electrons also experience the potential of the charged surface and lose energy as they approach the surface. **(b)** Energy distribution of the electron beam. Only the electrons with an energy higher than eV_p will reach the sample. The magnitude of this current I_{reach} is indicated by the blue area under the beam current density (equation 6.3).

poorly conducting PMMA layer is described by the Mott-Gurney law [10]:

$$I_p = \pm g V^2 \tag{6.1}$$

Where $g = \frac{9\epsilon\mu}{8d^3}$ (dielectric constant ϵ, carrier mobility μ and film thickness d). The minus sign applies for negative voltages. As the PMMA layer is illuminated, charge builds up on the surface until V_p is large enough for a current density I_p that is equal to the incoming beam current density I_0. Such an equilibrium, where the full beam current density, I_0, goes through the layer can only be reached when the initial electron energy, E_0, is sufficiently high. The charged surface does not only cause a current to flow through the resist layer, it also decelerates the incident electrons. The amount of energy an incoming electron loses on its way to the charged surface is determined by the surface potential. In the uncharged situation an electron would arrive with an energy $E_0 = 15$ keV $+ eV_{substrate}$. In the charged situation this will be $E_{land} = 15$ keV $+ eV_{surface}$ and therefore $E_{land} = E_0 - eV_p$. Only electrons with sufficient energy to overcome the surface potential (i.e. $E_{land} > 0$) will reach the resist layer (figure 6.2b). Since the electron beam has a certain energy width, part of the incident electron beam will be reflected before it reaches the sample (figure 6.2b). We approximate the energy distribution of the beam by a Gaussian. For an electron beam current I_0 with an average initial electron energy E_0 with a standard deviation σ, the current density (in Amps per eV) of the beam is given by:

$$\mathcal{I}(E) = \frac{I_0}{\sigma\sqrt{2\pi}} e^{-\frac{(E-E_0)^2}{2\sigma^2}} \tag{6.2}$$

The current that reaches the resist layer is therefore given by:

$$I_{reach}(V_p) = \frac{I_0}{\sigma\sqrt{2\pi}} \int_{eV_p}^{\infty} e^{-\frac{(E-E_0)^2}{2\sigma^2}} dE \tag{6.3}$$

Thus, the resist layer charges up to a potential V_p such that not the whole beam current has to flow through the layer, but only the current that reaches the surface, I_{reach}. The rest, $I_0 - I_{reach}$ is reflected back into the vacuum before it reaches the sample (figure 6.2). The surface potential that satisfies this condition, V_{eq}, can be found by setting I_{reach} equal to I_p:

$$\pm g_0 V_p^2 = \frac{1}{\sigma\sqrt{2\pi}} \int_{eV_p}^{\infty} e^{-\frac{(E-E_0)^2}{2\sigma^2}} dE \tag{6.4}$$

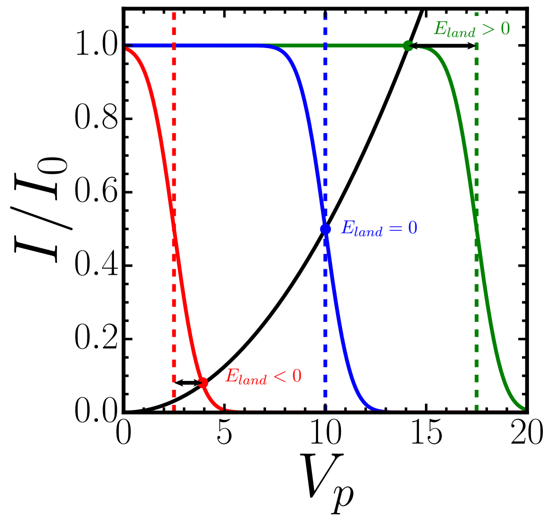

Figure 6.3: Depiction of equation 6.4. The black curve is the left-hand side of equation 6.4. Here we use $g_0 = 0.005$. The other curves are the right hand sides of equation 6.4 for different values of E_0 and $\sigma = 1$ eV. $E_0 = 2.5$ eV in red, $E_0 = 10$ eV in blue, and $E_0 = 17.5$ eV in green. The solutions of equation 6.4, V_{eq} for the different values of E_0, are indicated by the coloured dots. The vertical dashed lines represent the value of V_p for which $V_p = {}^{E_0}/_{e}$. E_{land} is the difference between E_0 and eV_{eq}, indicated with a double arrow. The value of E_0 for which half of I_0 reaches the sample, we call E_{th}. This is the case for $E_0 = 15$ eV. For $E_0 < E_{th}$ we find $E_{land} < 0$ and for $E_0 > E_{th}$ we find $E_{land} > 0$.

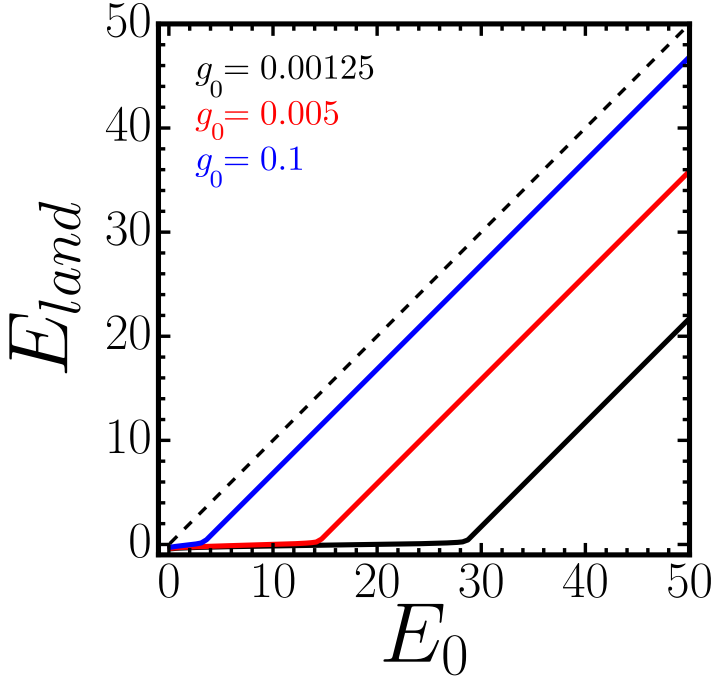

Figure 6.4: Effective landing energy, E_{land} as a function of E_0, with $E_{land} = E_0 - eV_{eq}$ where V_{eq} are the solutions of equation 6.4 with $\sigma = 0.125$ eV. E_{land} is plotted for a good conductor (dashed black line) and for a poor conductor (e.g. PMMA) for different beam currents, $g_0 = g/I_0 = 0.00125$ (black), 0.005 (red), and 0.1 (blue). For poor conductors we find the E_{land} is initially < 0 and becomes positive for $E_0 > E_{th}$. This shifting up of the threshold energy for high beam currents corresponds with our observations in the PMMA exposures (figure 6.1).

where $g_0 = g/I_0$. In figure 6.3 the left-hand side of equation 6.4 is represented by the black line with $g_0 = 0.005$ and the right-hand side by red, blue, and green lines for different values of E_0. The steady state (i.e. the solution of equation 6.4) is given by the intersections of the black and the coloured lines. At this equilibrium our charging model predicts an effective landing energy:

$$E_{land} = E_0 - eV_{eq} \tag{6.5}$$

which is graphically indicated in figure 6.3. In figure 6.4 E_{land} is plotted as a function of E_0 for different values of g_0. The dashed line represents the non-charging situation with $E_{land} = E_0$. The blue ($g_0 = 0.1$), red ($g_0 = 0.005$), and black ($g_0 = 0.00125$) lines represent the charging situation with a poor

conductor. These curves show that for low E_0, E_{land} increases only slowly. In this regime V_p is not large enough to give rise to a sufficiently large current through the PMMA to lead the full beam current away. A large fraction of the incident electrons is reflected before they reach the sample. The value of E_0 for which half of the incident current reaches the sample we call E_{th}. At some higher E_0 where $E_0 \geq E_{th}$, the electron energy is sufficient to create a potential that allows the full beam current to reach the PMMA. We see that E_{th} shifts to higher values as g_0 is decreased. Since $g_0 = g/I_0$, this is equivalent to a larger I_0. This shift in E_{th} with I_0 corresponds to our observations in figure 6.1.

6.2.1 Testing the charging model

In section 2.1.4 we explain how the dispersion of the magnetic prism array in the ESCHER setup can be used to determine the energy distribution of the electrons leaving the sample, with a technique called electron energy loss spectroscopy (EELS). In this distribution, electrons with the highest energy are the electrons with the smallest energy loss. Electrons with the lowest energy are those that are just able to overcome the work function and leave the material. The energy difference between highest- and lowest-energy electrons is equal to E_{land}. Since the magnetic prism spatially separates those electrons over a certain distance that linearly depends on the energy difference, we are able to determine E_{land} as a function of the initial electron energy, E_0, by measuring the energy spectrum of the electrons returning from the sample. This allows us to test the predictions of our simple charging model.

Figure 6.5a shows the energy spectrum of the electrons leaving a silicon sample, which is illuminated with 20 eV electrons. As expected, for a non-charging sample, we find $E_{land} = E_0$. This remains so for the entire duration of the experiment. Figure 6.5b shows the energy spectrum of the electrons leaving a PMMA surface that is illuminated with 20 eV electrons 200 ms after the beginning of the exposure. We find that $E_{land} = 25.8$ eV $> E_0$. Figure 6.5c shows the energy spectrum of electrons leaving the same area as in figure 6.5b, but 60 s after the beginning of the exposure. E_{land} is different than at the beginning of the exposure and we now find that $E_{land} = 14.5$ eV $< E_0$.

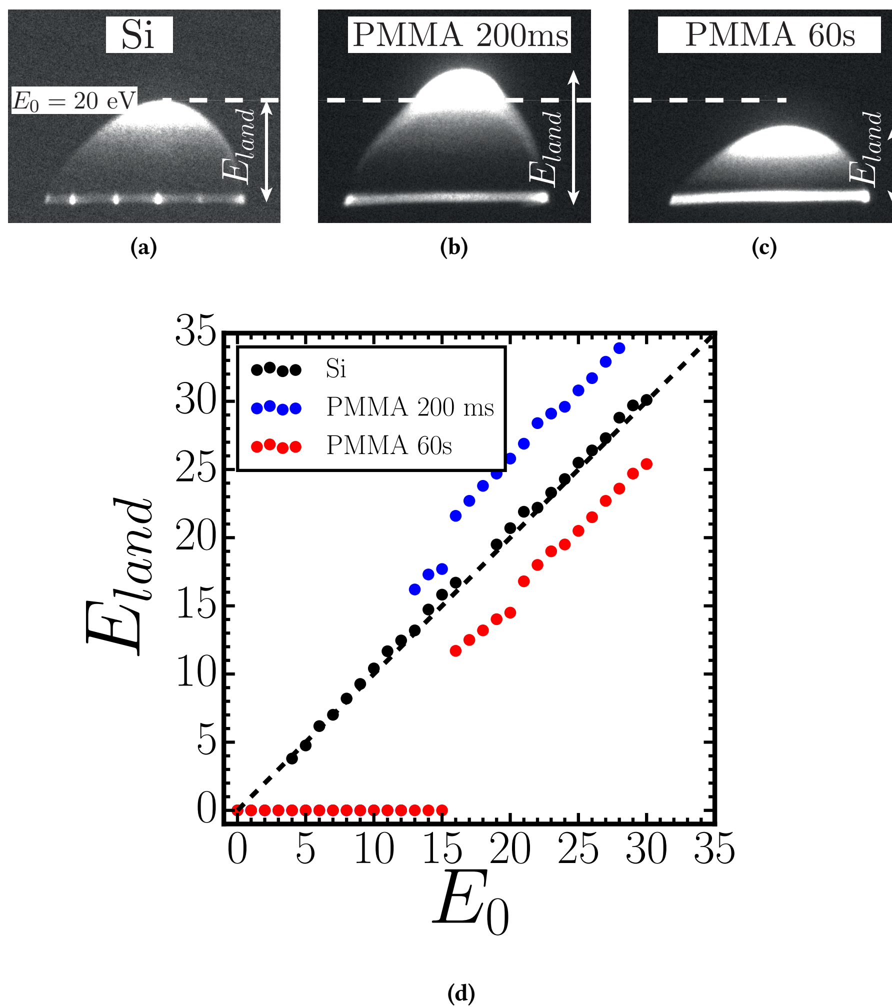

Figure 6.5: (a) EELS spectrum measured on Si with $E_0 = 20$ eV. We find $E_0 = E_{land}$. **(b)** EELS spectrum measured on PMMA after 200 ms after the beginning of the exposure with $E_0 = 20$ eV. We find $E_{land} = 25.8$ eV $> E_0$. **(c)** EELS spectrum measured on the same region in (b) after 60 s. We find $E_{land} = 14.5$ eV $< E_0$. **(d)** E_{land}, as a function of initial electron energy, E_0, measured on bare silicon (black dots), on PMMA E_{land} at 200 ms into the exposure (blue) and after 60 s (red).

In figure 6.5d we show E_{land}, measured on silicon (black), on PMMA after 200 ms (blue), and after 60 s (red) for different values of E_0 with a beam current $I_0 = 0.25$ nA . On the PMMA we find for $E_0 < 15$ eV that E_{land} is very low, just like the model predicts. However, above 15 eV the measured E_{land} dramatically deviates from our model (see figure 6.4). When E_0 is increased from a value below threshold to one above, E_{land} suddenly jumps to a value that is higher than E_0 (blue dots). Over some time, E_{land} decreases to a value below E_0 (red dots).

To further investigate the observed time dependence of E_{land}, we performed time-dependent measurements of E_{land} with a higher time resolution (figure 6.6 with a beam current 0.25 nA). In this figure the horizontal axis shows the energy loss and the vertical axis shows the time. In each time interval the EELS spectrum is integrated over a narrow slice around $\mathbf{k}_{\parallel} = 0$ and represented horizontally with the intensity in a color scale. The difference between the smallest and largest loss is equal to E_{land}.

Figure 6.6a shows the spectrum for $E_0 = 14$ eV, which is below the threshold energy. The effective landing energy stays ~ 0 eV for the full duration of the experiment. When $E_0 = 15$ eV, E_{land} is initially ~ 0 eV (figure 6.6b). After about 10 s, E_{land} starts to increase until it is almost equal to E_0. For larger values of E_0, in figure 6.6c ($E_0 = 20$ eV) we find different behaviour. At the beginning of the exposure E_{land} is higher than E_0 and after a certain amount of time we observe a sudden jump in E_{land}, suggestive of an instability in the system. In figures 6.6d ($E_0 = 25$ eV) and 6.6e ($E_0 = 30$ eV) there is a similar jump. However, at the beginning of the exposure there is a rapid decrease in E_{land}.

Even though the charging model predicts a threshold energy that depends on the beam current (figures 6.4 and 6.1), it cannot explain the observations in figures 6.5 and 6.6. The measurements show that the effective landing energy changes over time and sometimes suddenly jumps to different values. The observed behaviour is reminiscent of an unstable system. In the next section we argue that the behaviour is a consequence of secondary electron emission in combination with resist changes during radiation exposure due to radiation damage. The latter causes the conductivity and the secondary electron emission coefficient to change over time. With these modifications our model resembles something that in catastrophe theory is called a cusp catastrophe [11].

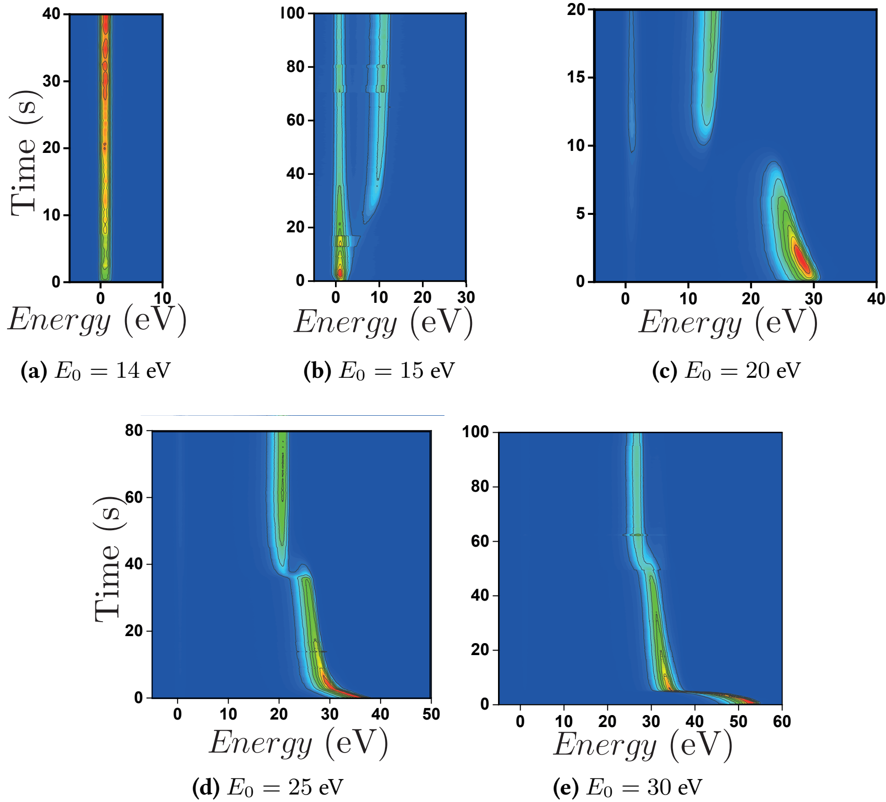

Figure 6.6: Measurement of E_{land} as a function of time for different values of E_0. In each figure the energy loss spectrum is plotted horizontally with the intensity on a color scale. **(a)** E_{land} measured for $E_0 = 14$ eV $< E_{th}$. Here the landing energy stays low for a long time. **(b)** Resist exposure for an energy above threshold $E_0 = 15$ eV. Initially the E_{land} is low. After some time E_{land} increases. **(c)** Exposure with $E_0 = 20$ eV electrons. E_{land} starts out at a value of ~ 30 eV which is about 10 eV higher than E_0. E_{land} initially gradually decreases. However, after ~ 10 s, E_{land} suddenly drops from about 25 eV to ~ 10 eV. This means that the resist switches from a positively charged to a negatively charged situation. **(d)**,**(e)** Exposure with $E_{land} = 25$ eV and $E_{land} = 30$ eV.

6.3 Secondary electron emission

The observed behaviour in figure 6.6 is clearly not predicted by a simple charging model. Our model does not take secondary electron emission (SEE) into account. To do this, we introduce the SEE coefficient. This coefficient is a measure of the number of secondary electrons released per incoming electron. The SEE coefficient is a function of incident electron energy, $\delta_s(E)$. This has been studied extensively [12–19], but is not well characterized below 100 eV. In this energy range we may approximate $\delta_s(E)$ by:

$$\delta_s(E) = \left(\frac{E}{E_1}\right)^\alpha \tag{6.6}$$

E_1 is the energy for which $\delta_s(E) = 1$. There is not much literature on the exact form of δ_s below 100 eV. We refer to the work of Scholtz et al. [20]. They give an empirical description of the secondary electron emission. They provide no justification, other than that it fits the data. We find that equation 6.6 has good overlap with their results for $1/2 < \alpha < 5/4$. Another empirical description is given by Burke et al. [21]. This description is also used by Lin et al. [22]. For PMMA we find a good overlap with their data with $\alpha = 0.85$ and $E_1 = 56.7$ eV (we will later find $E_1 = 18$ eV for PMMA). The literature does not provide any dose or time dependence (which we will find to be very important for E_1) and there is very little data below 50 eV. Thus, the precise form of $\delta_s(E)$ is largely conjecture. Equation 6.6 is used for the theoretical description of the secondary electron emission from insulating surfaces in Hall thrusters [23], a type of ion thruster used for spacecraft propulsion. Fortunately, our description that describes the observations in figure 6.6 is not very sensitive to the precise form of $\delta_s(E)$.

Since secondary electrons *leave* the sample, this effect reduces the net current that reaches the sample, I_{reach}. This means that equation 6.3 has to be modified. For an incident electron energy E and charging potential V_p, E_{land} is given by $E_{land} = E - eV_p$. The incoming current is therefore reduced by a factor $1 - \delta_s(E_{land})$. With this, equation 6.3 becomes:

$$I_{reach}(V_p) = \frac{I_0}{\sigma\sqrt{2\pi}} \int_{eV_p}^{\infty} \left(1 - \left[\frac{E - eV_p}{E_1}\right]^\alpha\right) e^{-\frac{(E-E_0)^2}{2\sigma^2}} dE \tag{6.7}$$

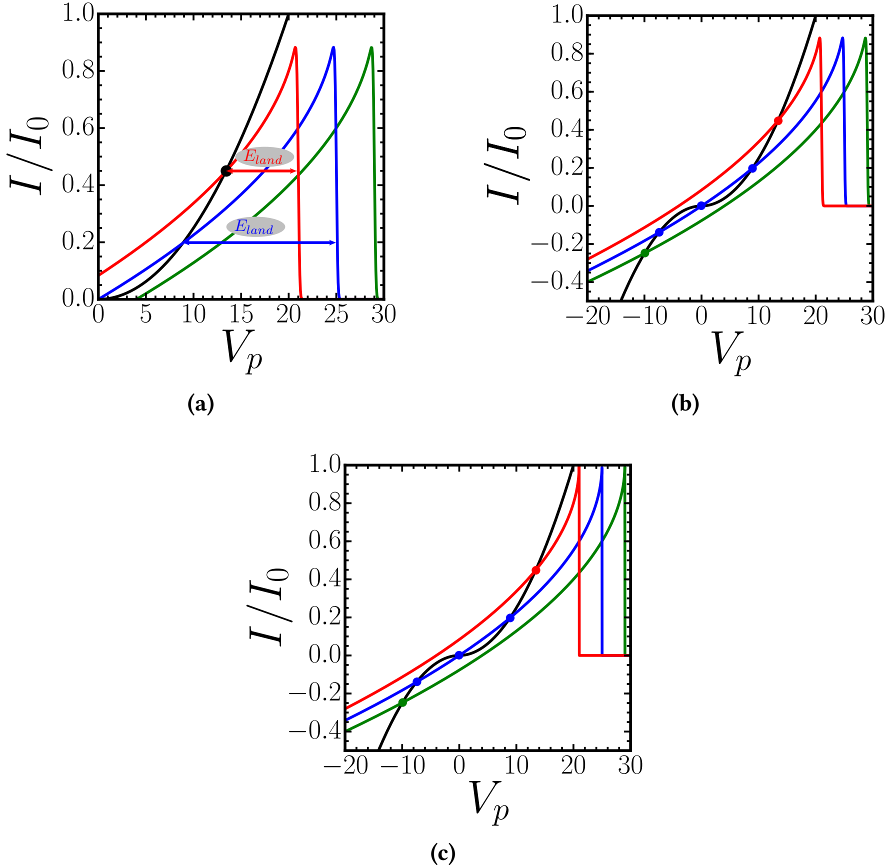

Figure 6.7: Depiction of equation 6.7 with the Mott-Gurney current through the PMMA (black line) with $g_0 = 0.0025$, as a function of V_p. **(a)** Very similar to figure 6.3 but now with secondary electron emission, with $E_1 = 25$ eV and $\alpha = 1/2$. I_{reach}/I_0 is plotted as a function of the charging potential V_p for three different initial electron energies: $E_0 = 21$ eV (red), $E_0 = 25$ (blue), and $E_0 = 29$ eV (green) with $\sigma = 0.125$ eV. Since secondary electrons leave the sample, SEE reduces the net current reaching the sample. The landing energy is the difference between E_0 and eV_{eq}, indicated with a double arrow. For $E_0 = 25$ eV the effective landing is larger than in the $E_0 = 20$ eV situation. For $E_0 = 29$ eV we find that $V_{eq} < 0$. This can be seen in **(b)** which also shows that in the $E_0 = 25$ eV situation, there are three possible solutions for E_{land}. **(c)** similar to (b), but now with $\sigma = 0$. This represents equation 6.9.

Figure 6.7a shows the current that reaches the layer as a function of the charging potential V_p. Comparison with figure 6.3 shows the importance of including SEE in the model. I_{reach} is shown for three different values of E_0: 21, 25, and 29 eV. E_{land} for $E_0 = 21$ eV, is smaller than the E_{land} found for $E_0 = 25$ eV. The secondary electron emission is higher in the latter case, resulting in a lower current reaching the sample. It also becomes clear why the results presented in figure 6.5d are only in accordance with the model without SEE for values of E_0 *below* the threshold energy. Below the threshold energy, E_{land} is almost 0, there is therefore no SEE and the previous model is thus sufficient to describe those results.

Equation 6.7 can be simplified by assuming an infinitely narrow energy distribution of the incoming electron beam (a delta function). This is a good approximation because the electron beam used in our experiments has a σ of ~ 0.1 eV, which is small compared to the relevant energies in the experiment (this can be seen by comparing figures 6.7b and 6.7c). With this assumption equation 6.7 becomes:

$$\frac{I_{reach}}{I_0} = 1 - \left(\frac{E_0 - eV_p}{E_1}\right)^{\alpha} \tag{6.8}$$

The charging potential to which the sample charges up, V_p, is again the potential for which the current reaching the sample equals the current through the PMMA layer. This potential can therefore be found by solving:

$$\pm g_0 V_p^2 = 1 - \left(\frac{E_0 - eV_p}{E_1}\right)^{\alpha} \tag{6.9}$$

for V_p. The minus sign on the left-hand side is for $V_p < 0$. The left-hand side of this equation is represented by the black dashed line in figure 6.7c and the right-hand side (with $\alpha = 1/2$) for different values of E_0: 21 (red), 25 (blue), and 29 eV (green). For $E_0 = 21$ eV there is one solution, indicated by the red dot, for which $E_{land} = E_0 - eV_{eq} < E_0$. For $E_0 = 29$ eV there is also one solution, indicated by the green dot. Interestingly here $E_{land} > E_0$, corresponding to positive charge accumulation on the surface. Finally, we see that $E_0 = 25$ eV has *three* possible solutions for E_{land}.

In the $E_{land} > E_0$ situation more electrons leave the surface than reach it via the incident beam current. This happens when each incident electron causes the emission of more than one secondary electron. This leads to a positive charge build-up on the surface which gives rise to a current in which electrons

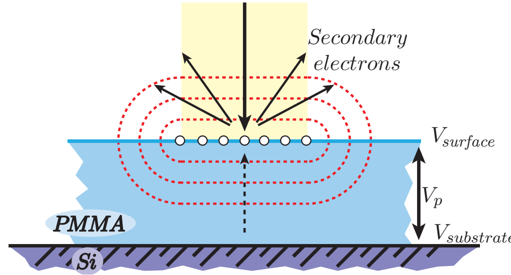

Figure 6.8: Schematic representation of the $V_{eq} < 0$ situation that corresponds to a positive charge build up on the resist surface. When $\delta_s > 1$ more than one secondary electron is generated per incoming electron, i.e., more electrons leave the resist surface than reach it via the beam current. The positive charge built up on the resist accelerates incoming electrons towards the surface and it causes a current flow in the resist in which electrons flow from the Si substrate towards the surface (indicated by the dashed arrow (n.b. it points in the direction in which electrons move)).

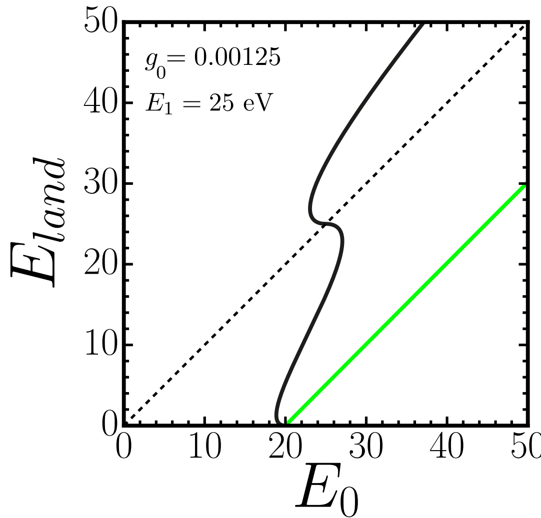

Figure 6.9: $E_{land} = E_0 - eV_{eq}$ as a function of E_0 determined with the solutions from equation 6.9, for $g_0 = 0.00125$ with $E_1 = 25$ eV (black) and for $E_1 \to \infty$ (green). The black dashed line represents the non-charging situation.

flow from the substrate to the resist surface. This way a steady state can be sustained, as depicted in figure 6.8. Such a positively charged surface will accelerate electrons* towards it, causing them to land with a higher energy than in the non-charging case. This explains our observations presented in figure 6.6c, d, and e where we measured a landing energy, E_{land}, higher than E_0.

In figure 6.9 we plot the effective landing energy $E_{land} = E_0 - eV_{eq}$ determined from the solutions of equation 6.9, as a function of E_0, with $E_1 = 25$ eV, $g_0 = 0.00125$ and $\alpha = 1/2$ (black curve). We see that the curve has an s-shape due to the multiple solutions around $E_0 \approx E_1$. For $E_0 \lessapprox E_1$ we find that $E_{land} < E_0$, the landing energy is smaller than in the no-charging situation (black dashed line). For $E_0 \gtrapprox E_1$ we find $E_{land} > E_0$. When there is no SEE, $E_1 \to \infty$ (the green line), the sample also charges to 20 eV, beyond which E_{land} increases linearly with E_0 (just like in figure 6.4).

To explain the changing E_{land} in figure 6.6, however, resist changes during radiation exposure due to radiation damage should be accounted for in the model.

6.4 Resist changes due to radiation exposure

The effective electron landing energy, in figure 6.5d, exhibits time dependence and shows abrupt change from a positive to a negative charging state. This is a consequence of exposure induced changes in the SEE (via E_1) and the conductance (via g_0) of the PMMA layer, i.e. changes in the material because of radiation exposure.

Changes in SEE during electron exposure are well documented: bond breaking leads to the creation of charge traps which capture secondary electrons and reduce SEE (i.e. an increased E_1) [19]. Similarly, trap creation leads to doping of the PMMA, and increases the conductance during exposure.

*In our case a positively charged surface means that the electrons are decelerated less in the cathode lens configuration.

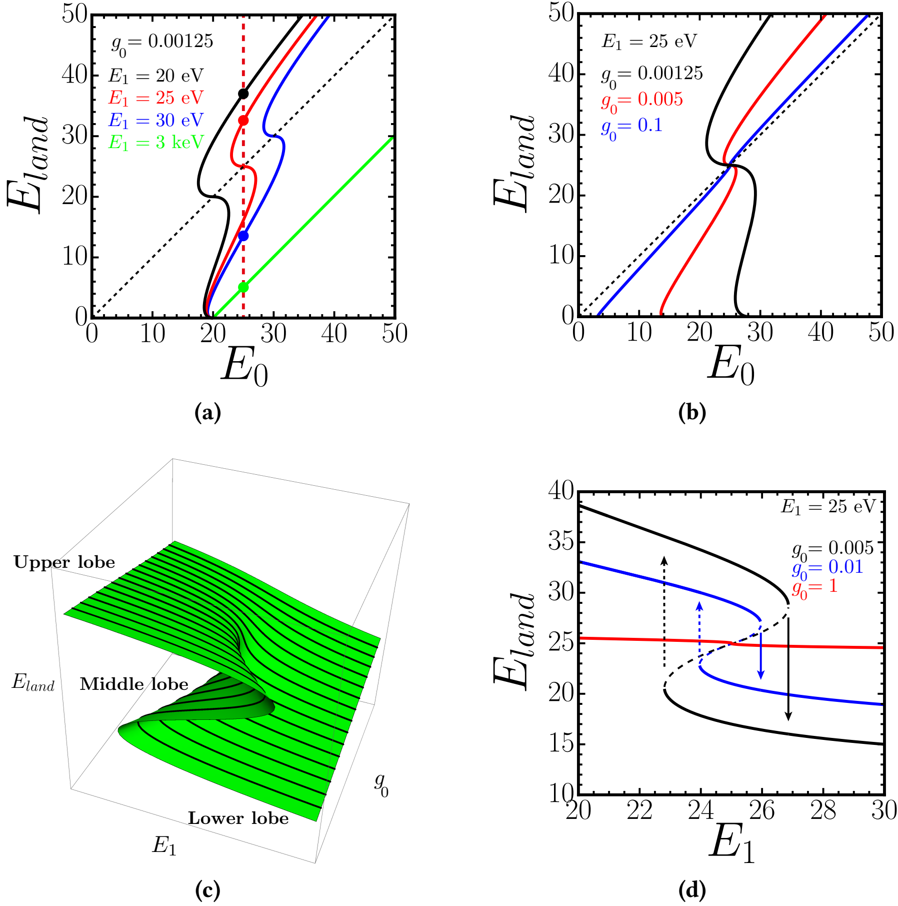

Figure 6.10: Influence the E_1 and g_0 on the E_{land} curves. **(a)** E_{land} curve for different values of E_1. The black, red, blue and green curves are E_{land} curves for different values of E_1 and $\alpha = 1/2$. **(b)** The effect of g_0 on the s-curves, also with $\alpha = 1/2$. N.b. $g_0 = g/I_0$ depends both on the conductivity of the material, g, and the beam current, I_0. **(c)** Schematic representation of the solutions of equation 6.9. **(d)** Solutions of equation 6.9 for different values of g_0: $g_0 = 0.005$ (black), $g_0 = 0.01$ (blue), and $g_0 = 1$ (red) with $\alpha = 1$.

In figure 6.10 we see the effect of these changes on the s-curves. When E_1 increases, the s-curve shifts to the right. In figure 6.10a we depict the effect of a changing E_1 on E_{land} for a fixed E_0. The initial situation, with $E_1 = 20$ eV, is presented by the black curve. The solution for E_{land} for $E_0 = 25$ eV (the red dashed line) is marked by a black dot. When E_1 is increased to a value of 25 eV, E_{land} (the red dot) continuously decreases. However, when E_1 is increased enough, the s-curve shifts past the $E_0 = 25$ eV line. E_{land} makes a discontinuous jump from the upper, to the lower branch (blue dot). This means that charging abruptly changes sign upon a continuous shift of E_1 during electron exposure.

Also, g_0 can also be changed to mimic the effect of a change (increase) of conductance over time. In figure 6.10b we increase g_0 from 0.00125 to 0.1. Increasing g_0 corresponds increasing the conductivity, or decreasing I_0. For $g_0 = 0.1$ we find a low E_{th} of ~ 3 eV. The black dashed line represent the no-charging situation ($g_0 \to \infty$). For lower g_0, E_{th} increases (again in agreement with our findings in figure 6.1) and the s-shape becomes more pronounced. These phenomena are examples of a cusp catastrophe.

The cusp catastrophe is a specific example of an unstable situation found in catastrophe theory [11]. It is an example of a bifurcating mathematical system in which continuous changes in the parameters can give rise to discontinuous ('catastrophical') changes in the system. It is usually defined by a potential function of the form $F(x; a, b) = {}^1\!/_4 x^4 + {}^1\!/_2 a x^2 + bx = 0$, where a and b are the so-called control parameters. $F(x; a, b)$ defines an equilibrium surface by the condition $\partial F/\partial x = 0$. This equilibrium surface contains a fold, as shown in figure 6.10c. Such a fold appears in many different functions. Specifically, equation 6.9 generates a folded surface, similar to F, with g_0 and E_1 playing the roles of a and b. In figure 6.10c a schematic representation of equation 6.9 is presented. Several regions can be distinguished here: an upper, a middle and a lower lobe. The black lines are solutions with constant g_0 and changing E_1, at a fixed value of E_0. Three of those solutions are plotted in figure 6.10d. These are solutions of equation 6.9 for $g_0 = 0.005$ (black), $g_0 = 0.01$ (blue), and $g_0 = 1$ (red) with $\alpha = 1$ and $E_0 = 25$ eV. If we start at a location on the upper lobe and increase E_1 (i.e. move to the right), we stay on the upper lobe, until we reach the edge of the lobe. If E_1 is increased further, there will be a discontinuous jump (drop) in E_{land} to the lower lobe. Vice versa, when we start on the lower lobe and decrease E_1 (move to the left) we stay on the lower lobe, until we reach the edge of the fold where we jump to the upper lobe

(this does not happen in the case of PMMA, as the damage (an increased E_1) in irreversible). The height of the jump is determined by g_0, we see that for $g_0 = 1$ the fold has practically disappeared and there is no more discontinuity as g_0 is increased further.

In figure 6.11 we use equation 6.9 to fit the results from the time dependent measurements of E_{land} in figure 6.6. This is done by linearly changing g_0, and E_1, as a function of time. g_0' and E_1' are the change rates. In figure 6.11b only g_0 is changed. Here E_0 is close to the threshold energy and E_{land} is thus not very sensitive to SEE. In figures 6.11c, 6.11d and 6.11e both E_0 and g_0 increase with time. In figures 6.11b and 6.11c the fits start with $g = 0.0025$ and $E_1 = 18$eV, and end with $g_0 = 0.025$ and $E_1 = 36$ eV (in 6.11c). This is 10-fold increase in conductance and a doubling of E_1.

During the exposures with $E_0 = 25$ eV and 30 eV (figures 6.11d and 6.11e) we observe a rapid decrease in E_{land} during the first few seconds that is not reproduced by the fits. Figure 6.11d starts at $E_{land} = 40$ eV, that is $V_p = 15$ V and $V_p = 25$ V in figure 6.11e*. Since V_p is the potential difference over a 20 nm thick resist layer, this corresponds to field strengths of 5 MVcm^{-1} in b, 7 MVcm^{-1} in c, 7.5 MVcm^{-1} in d, and 12.5 MVcm^{-1} in e.

We only find this initial rapid decrease in E_{land} when the field strength exceeds 7 MVcm^{-1}. At such strong fields the PMMA films can undergo dielectric breakdown, which alters the material properties. This happens until the PMMA film becomes sufficiently conductive to reduce V_p which stops the breakdown after which the processes previously described take over. Neusel et al. report a breakdown strength of 3.1 MVcm^{-1} [24]. We find a breakdown strength of > 7 MVcm^{-1}, more than twice as high.

Interestingly, we see that even in figure 6.11b, where $E_{land} \approx 0$, the resist undergoes changes in g_0. This indicates that even electrons close to 0 eV can damage the resist. Because an electron gains energy when it enters a material, this means an energy transfer of maximally the work function of the material which is ~ 4 eV. Furthermore we see that the rates of change in g_0 and E_1 do not depend strongly on electron energy. In figure 6.11b where $E_{land} \approx 0$, g_0 increases only a factor 2 slower than for $E_{land} \approx 30$ eV (figure 6.11e). In figures 6.11d and d6.11e the rates are somewhat smaller after the initial breakdown induced changes.

*This is again consistent with the initial values $g_0 = 0.0025$ and $E_1 = 18$ eV.

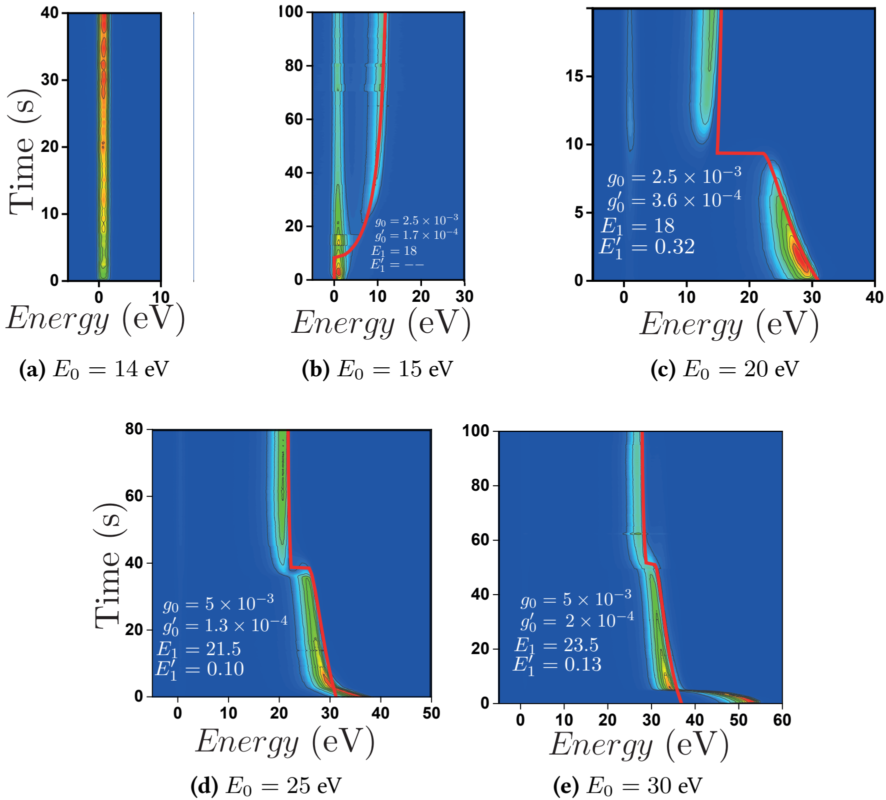

Figure 6.11: E_{land} fits from the charging model with SEE fitted to the time dependent E_{land} measurements. **(a)** $E_0 = 14$ eV, no resist change is observed and E_{land} therefore stays small. **(b)** $E_0 = 15$ eV only g_0 is changed to fit the data. Surprisingly, g_0 changes when $E_{land} \approx 0$. **(c)** $E_{land} = 20$ eV both E_1 and g_0 are changed to fit the measured data. **(d)** and **(e)** $E_0 = 25$ and 30 eV. The model is in good agreement with most of the curve but it does not include the sudden drop in E_{land} in the beginning of the exposure.

6.5 Summary

Our analysis of the LEE PMMA exposures reveals a wealth of information:

- During electron exposure the PMMA surface charges due to limited conductance.
- Charging can be either positive or negative, with a change in sign when $E_0 \approx E_1$ (figure 6.10d). The initial value of $E_1 = 18$ eV (figures 6.11b and 6.11c) is more than 3 times lower than literature suggests [14], and increases during electron exposure.
- Changes in g_0 and E_1 during exposure result in charging instabilities with a sudden change in the sign of V_p when E_1 becomes greater than E_0. A cusp catastrophe in equation 6.9 is responsible for these instabilities.
- Electrons with $E_{land} \approx 0$ eV already expose PMMA (figure 6.11b); g_0 increases at roughly the same rate for $E_{land} \approx 0$ eV, as for $E_{land} \approx 15$-35 eV. **D**issociative **E**lectron **A**ttachment (DEA) likely plays an important role in determining **L**ine **E**dge **R**oughness (LER), proximity effects, dose efficiency, and other effects in EUV and electron lithography.
- At field strengths > 7 MVcm^{-1} (20 nm PMMA) dielectric breakdown gives rise to a rapid increase in g_0 and E_1 during the first few seconds of exposure.

While all the presented results are on PMMA, experiments in exploratory EUV resists containing Sn(oxo) cages [25] show the same effects: sensitivity to ~ 0 eV electrons and strong charging instabilities. Since Sn(oxo) resists are very different from PMMA, this shows that the same basic principles apply. The experimental and theoretical methodology developed here will make it possible to study such EUV resists in more detail. The results of such studies can contribute to their characterization and optimization.

Surface charging might not be a very surprising effect in an electron microscope. However, when an insulating material is irradiated with high-energy photons as is done in EUV lithography, secondary electrons also leave the material. This could therefore cause the resist to charge up during exposure,

and lead to strong electric fields in the resist. During spatially patterned illumination, charging will also vary spatially and electric fields will develop both normal and parallel to the surface. This will have consequences for the pattern definition and line edge roughness in lithography applications. Surface charging, time dependence (i.e. dose) in the material properties of the resist (conductance and secondary electron emission), charging instabilities, and dielectric breakdown are not routinely considered in simulations of resist exposure, nor is the role of low-electron energy processes such as DEA [9, 26].

Furthermore, the methods we presented do not only allow us to study the effects of radiation damage in many more materials. It also allows us to determine conductivity properties of poorly insulating materials that are difficult to measure with other techniques as well as secondary electron emission. All of this is combined with the high resolution provided by the ESCHER microscope.

References

1. Thete A., Geelen D., van der Molen S. J. & Tromp R. M. Charge Catastrophe and Dielectric Breakdown During Exposure of Organic Thin Films to Low-Energy Electron Radiation. *Physical Review Letters* **119,** 266803 (2017).
2. Smith D. A., Fowlkes J. . & Rack P. D. A nanoscale three-dimensional Monte Carlo simulation of electron-beam-induced deposition with gas dynamics. *Nanotechnology* **18,** 265308 (2007).
3. Thete A., Geelen D., Wuister S., van der Molen S. J. & Tromp R. M. *Low-energy electron (0-100eV) interaction with resists using LEEM* in *Proceedings of SPIE - The International Society for Optical Engineering* (eds Wood O. R. & Panning E. M.) **9422** (2015), 9422. ISBN: 9781628415247.
4. Wollersheim O., Zumaqué H., Hormes J., Kadereit D., Langen J., Häußling L., Hoessel P. & Hoffmann G. Quantitative studies of the radiation chemical behaviour of PMMA and poly(lactides). *Nuclear Instruments and Methods in Physics Research Section B: Beam Interactions with Materials and Atoms* **97,** 273–278 (1995).
5. Hiraoka H. Radiation Chemistry of Poly(methacrylates). *IBM Journal of Research and Development* **21,** 121–130 (1977).
6. Lehockey E. M., Reid I. & Hill I. The radiation chemistry of poly(methyl methacrylate) polymer resists. *Journal of Vacuum Science & Technology A: Vacuum, Surfaces, and Films* **6,** 2221–2225 (1988).
7. Yates B. W. & Shinozaki D. M. Radiation degradation of poly(methyl methacrylate) in the soft x-ray region. *Journal of Polymer Science Part B: Polymer Physics* **31,** 1779–1784 (1993).
8. *The Radiation Chemistry of Macromolecules Volumes I and II* (ed Dole M.) (Academic Press, 1972).
9. Rangan S., Bartynski R. A., Narasimhan A. & Brainard R. L. Electronic structure, excitation properties, and chemical transformations of extreme ultra-violet resist materials. *Journal of Applied Physics* **122,** 025305 (2017).
10. Pope M. & Swenberg C. E. *Electronic Processes in Organic Crystals and Polymers* 1328. ISBN: 0195129636 (Oxford University Press, 1999).
11. Gilmore R. *Catastrophe Theory for Scientists and Engineers*‘ ISBN: 9780471050643 (Wiley & Sons, 1981).

12. Joy D. C., Prasad M. S. & Meyer H. M. Experimental secondary electron spectra under SEM conditions. *Journal of Microscopy* **215,** 77–85 (2004).
13. Cazaux J. e-Induced secondary electron emission yield of insulators and charging effects. *Nuclear Instruments and Methods in Physics Research Section B: Beam Interactions with Materials and Atoms* **244,** 307–322 (2006).
14. Burke E. A. Secondary Emission from Polymers. *IEEE Transactions on Nuclear Science* **27,** 1759–1764 (1980).
15. Scholtz J., Dijkkamp D. & Schmitz R. Secondary electron emission properties. *Philips Journal of Research* **50,** 375–389 (1996).
16. Lin Y. & Joy D. C. A new examination of secondary electron yield data. *Surface and Interface Analysis* **37,** 895–900 (2005).
17. Said K., Damamme G., Si Ahmed A., Moya G. & Kallel A. Dependence of secondary electron emission on surface charging in sapphire and polycrystalline alumina: Evaluation of the effective cross sections for recombination and trapping. *Applied Surface Science* **297,** 45–51 (2014).
18. Ganachaud J. & Mokrani A. Theoretical study of the secondary electron emission of insulating targets. *Surface Science* **334,** 329–341 (1995).
19. Dapor M., Ciappa M. & Fichtner W. Monte Carlo modeling in the low-energy domain of the secondary electron emission of polymethylmethacrylate for critical-dimension scanning electron microscopy. *Journal of Micro/Nanolithography, MEMS, and MOEMS* **9,** 023001 (2010).
20. Scholtz J., Dijkkamp D. & Schmitz R. Secondary electron emission properties. *Philips Journal of Research* **50,** 375–389 (1996).
21. Burke E. A. Secondary Emission from Polymers. *IEEE Transactions on Nuclear Science* **27,** 1759–1764 (1980).
22. Lin Y. & Joy D. C. A new examination of secondary electron yield data. *Surface and Interface Analysis* **37,** 895–900 (2005).
23. Dunaevsky A., Raitses Y. & Fisch N. J. Secondary electron emission from dielectric materials of a Hall thruster with segmented electrodes. *Physics of Plasmas* **10,** 2574–2577 (2003).
24. Neusel C. & Schneider G. A. Size-dependence of the dielectric breakdown strength from nano- to millimeter scale. *Journal of the Mechanics and Physics of Solids* **63,** 201–213 (2014).

25. Cardineau B., Del Re R., Al-Mashat H., Marnell M., Vockenhuber M., Ekinci Y., Sarma C., Neisser M., Freedman D. A. & Brainard R. L. *EUV resists based on tin-oxo clusters* in (eds Wallow T. I. & Hohle C. K.) (2014), 90511B.
26. Wiseheart L., Narasimhan A., Grzeskowiak S., Neisser M., Ocola L. E., Denbeaux G. & Brainard R. L. *Energy deposition and charging in EUV lithography: Monte Carlo studies* in (eds Panning E. M. & Goldberg K. A.) (2016), 97762O.